Materials Science & Engineering A 871 (2023) 144886

Contents lists available at ScienceDirect

Materials Science & Engineering A

journal homepage: www.elsevier.com/locate/msea

Laser shock peening strengthens additively manufactured high-entropy alloy through novel surface grain rotation

Yunjian Bai [a,c,1], Guo-Jian Lyu [b,1], Yun-Jiang Wang [b,c], Tianyu Chen [a], Kun Zhang [a,c,*], Bingchen Wei [a,c,d,**]

[a] Key Laboratory of Microgravity (National Microgravity Laboratory), Institute of Mechanics, Chinese Academy of Sciences, Beijing, 100190, China
[b] State Key Laboratory of Nonlinear Mechanics, Institute of Mechanics, Chinese Academy of Sciences, Beijing, 100190, China
[c] School of Engineering Science, University of Chinese Academy of Sciences, Beijing, 100049, China
[d] Center of Materials Science and Optoelectronics Engineering, University of Chinese Academy of Sciences, Beijing, 100049, China

ARTICLE INFO

Keywords:
High-entropy alloy
Additive manufacturing
Laser shock peening
Grain refinement
Dislocation slip

ABSTRACT

Additive manufacturing has flourished as an advanced technique to process metals and alloys. However, this strategy usually introduces undesired defects that deteriorates the mechanical performance of structural materials. Herein laser shock peening (LSP) is proposed as an efficient strengthening approach to reshape the surface morphology of a prototypical dual-phase AlCoCrFeNi high-entropy alloy (HEA) after additive manufacturing, in which remarkable strengthening is achieved. Combined electron back scatter diffraction and transmission electron microscope characterizations reveal that the mechanical enhancement is attributed to the grain refinement and accumulation of dislocations at the impact surface. In extreme condition of LSP, the grain refinement is not accommodated by the conventional dynamic recrystallization anymore, but a novel mechanism of parental columnar grain rotation which can be rationalized by a continuum-level theory from a geometrical perspective. The new mechanism is verified by large-scale atomistic simulations which further recognizes the critical role of multiple unstable dislocation slip and amorphization in formation of smaller grains under shock. Our strategy offers a promising pathway toward polishing morphology of HEAs and thus, prohibiting the potential intrinsic defected induced-mechanical degradation of the additively manufactured metals and alloys via novel microscopic mechanism.

1. Introduction

The birth of high-entropy alloys (HEAs) has attracted considerable attention in vast communities of materials and physics in the past decades [1–7]. It triggers a completely new design concept of physical metallurgy [1], that is, HEAs contain at least four elements in equal or near equal ratios (i.e., multiple principal elements). This innovation greatly expands the design phase space for metallic materials [4,6], and brings about excellent mechanical performances of this new type of alloys in a wide range of service conditions from cryogenic to elevated temperatures [8–10] that potentially finds their applications in severe engineering conditions.

Thanks to their competitive mechanical properties, HEAs are expected as promising structural materials [11,12]. However, the limitations – including fluidity, geometry and scale – of the conventional manufacturing methods such as casting make it difficult to prepare HEAs components in real apparatus. Additive manufacturing has flourished as an advanced technique to process metals and alloys [13–20]. In addition, additive manufacturing is particularly suitable for fabrication of the large-scale parts with complex geometries, which is therefore deemed as a powerful tool to prepare HEAs structural materials [21]. Additive manufacturing appears to yield superior mechanical properties. For instances, the additively manufactured Damascus steel [22], Ti alloy [23] and Al alloy [24] exhibit very high strength, and the

* Corresponding author. Key Laboratory of Microgravity (National Microgravity Laboratory), Institute of Mechanics, Chinese Academy of Sciences, Beijing, 100190, China.
** Corresponding author. Key Laboratory of Microgravity (National Microgravity Laboratory), Institute of Mechanics, Chinese Academy of Sciences, Beijing, 100190, China.
E-mail addresses: zhangkun@imech.ac.cn (K. Zhang), weibc@imech.ac.cn (B. Wei).
[1] These authors contribute equally to this work.

https://doi.org/10.1016/j.msea.2023.144886
Received 30 January 2023; Received in revised form 4 March 2023; Accepted 5 March 2023
Available online 17 March 2023

additively manufactured Al–12Si alloy simultaneously improves the strength and toughness [25]. Nonetheless, additive manufacturing often leads to intrinsic defects such as micro-cracks, various types of voids [26,27] and exclusively columnar grains [23,24]. These representative defects may not be completely eliminated through processing optimization due to the specific solidification conditions, which results in limitations with respect to various mechanical properties and loading paths, thereby preventing additive manufacturing of metals and alloys from reaching their full potential [24]. Hence, additional employed post-processing is required to improve the printing process-related attributes.

Laser shock peening (LSP) offers a valuable opportunity to modify or reshape the surface morphology of the metallic materials parts with complex geometries, and subsequently further effectively strengthens the targets. LSP has been demonstrated to significantly improve the fatigue life [28,29], corrosion resistance [30] and hardness [31,32] of the conventional metallic materials. It is also found that LSP treatment can greatly improve the yield strength and tensile plasticity of a face-centered cubic (FCC) CrFeCoNiMnCu HEA by producing proper structural gradient [33]. In addition to the performance enhancement, various strengthening mechanisms through LSP have been proposed from a fundamental study perspective, including compressive residual stress strengthening [34], dislocation hardening [31], precipitation strengthening [29], grain refinement strengthening [32], etc. However, whether LSP is efficacious for improving the mechanical performance of the additively manufactured HEAs, in particular, the brittle body-centered cubic (BCC) phase HEAs, remains open, owing to the representative columnar grain structure. If so, the microscopic mechanism is still unclear. Although Tong et al. [35] demonstrated that LSP can improve the strength and plasticity of the additively manufactured CoCrFeNiMn HEA, the HEA was not a typical columnar crystal structure [36], and therefore, the above questions remain difficult to answer. One could naturally raise a question whether the existing microscopic mechanism of strengthening in conventional materials remains appropriate in the additively manufactured HEAs after LSP in which strong chemical complexity, severe lattice distortion and typical columnar grains exist.

To answer these questions, LSP was conducted in an additively manufactured AlCoCrFeNi HEA. The laser shock peened HEA exhibits improved hardness, ultimate strength, and compressive ductility. Systematical structural characterization, including texture, dislocation, grain morphology was performed, which reveals a novel deformation mechanism of grain refinement via parental columnar grain rotation under laser shock that can be verified by microscopic molecular dynamics simulations and interpreted by a theoretical model. These insights facilitate to establish a bottom-up approach to enhance the mechanical performance of additively manufactured HEAs via LSP.

2. Experimental procedure

2.1. Material preparation

The pre-alloyed powder was prepared via vacuum induction melting gas atomization. The size of powder was controlled from 45 μm to 105 μm. The chemical composition counted by atomic ratio of the powder was listed in Table 1 along with their atomic radius. As-printed samples with a 10 mm × 10 mm × 10 mm dimension were prepared by a LENS-450 3D-printing machine (direct energy deposition pattern) with argon atmosphere protection. A series of optimizations have been carried out before the final printing parameters were determined. The laser power was 300 W, and the scanning speed is 530 mm/min. Laser beam diameter was ~260 μm. The layer thickness was ~250 μm. A bidirectional scanning strategy was used, in which the scanning direction between the two adjacent layers was perpendicular.

Table 1
The elemental composition and atom radius of the AlCoCrFeNi HEA.

Element	Al	Co	Cr	Fe	Ni
Concentration c_i	0.21 ± 0.08	0.15 ± 0.03	0.18 ± 0.03	0.16 ± 0.03	0.30 ± 0.03
Radius r_i (Å)	1.43	1.26	1.27	1.27	1.24

2.2. Laser shock peening and mechanical tests

A specimen of dimension 10 mm × 10 mm × 3 mm dimensions was cut from the cubic sample by the electrical discharge machining. The specimen was polished to remove possible surface defects and prepared for subsequent LSP treatment. A Q-switched Nd: YAG pulse laser with ~1064 nm wavelength was utilized to impact the specimen. The laser energy was ~1.32 J, and the diameter of the focused laser spot was ~2 mm. The confining medium and ablative layer were purified water and aluminum foil, respectively. The laser shock propagation is parallel to the building direction (BD). The mechanical property was measured by nanoindentation test, which was carried out at room temperature using Nano Indenter G200 with a Berkovich diamond indenter. The loading force is 10 mN; the loading and unloading speed is both 0.5 mN/s; the holding time is 10 s. The indentation contact projection area is on the order of microns, which is far larger than the phase size of both the BCC and B_2 (~80 nm width in Fig. 1c). Therefore, the obtained hardness value in Fig. 2b is the average value of the HEA. A grid indentation was performed, and the step length along the LSP impact direction is 30 μm and the step length perpendicular to the impact direction is 50 μm. Cylindrical specimens for compression were cut to Φ5 × 10 mm. The sides of the cylindrical specimens were subjected to LSP by rotating the samples continuously. Compressive tests were performed an LD26 universal testing machine upon a steady strain rate of 1×10^{-3} s^{-1} at room temperature. At least three times for samples in each condition were tested to ensure repeatability.

2.3. Microstructural characterization

X-ray diffraction (XRD) pattern with Cu-Kα radiation (Smartlab 9 kW) was used to identify the phase composition of the as-printed sample. The scanning angle was from 20° to 100° with a step 0.05°. The scanning electron microscope (SEM JSM-7100F) equipped with electron backscatter diffraction (EBSD) was used to characterize the microstructure of the printed HEA before and after LSP. The samples for EBSD observations were prepared by vibration polishing. The EBSD scanning step size is 0.7 μm. The atomic scale structure and crystalline defect in the specimen before and after LSP were further observed by transmission electron microscope (TEM) using JEOL JEM-2100F field emission instrument operating at 200 kV. The deformed TEM sample was accurately prepared by the focused ion beam (FEI-Scios2).

2.4. Molecular dynamics

Molecular dynamics (MD) simulations were carried out to mimic the laser shock peening process on the same HEA using the open-source code LAMMPS (Large-scale Atomic/Molecular Massively Parallel Simulator) [37]. The atomistic model consists of both B_2–AlNi and BCC-FeCr phases with 14 (7 + 7) columnar grains that created by the ATOMSK code [38] with random crystalline orientations. The large-scale model contains 10,465,883 atoms, which are described by an *ad hoc* empirical hybrid potential. Atomic interactions between Al and Ni atoms, as well as that between Fe and Cr atoms are described by the existing embedded atomic method (EAM) potentials developed by Mishin et al. [39] and Eich et al. [40], respectively. The remaining interactions between other atom pairs are described by another EAM potential proposed by Farkas et al. [41]. After fabrication, the sample was first relaxed at 300 K and zero pressure for 0.5 ns with periodic boundary conditions in a constant pressure and constant temperature ensemble. To mimic the process of LSP, the

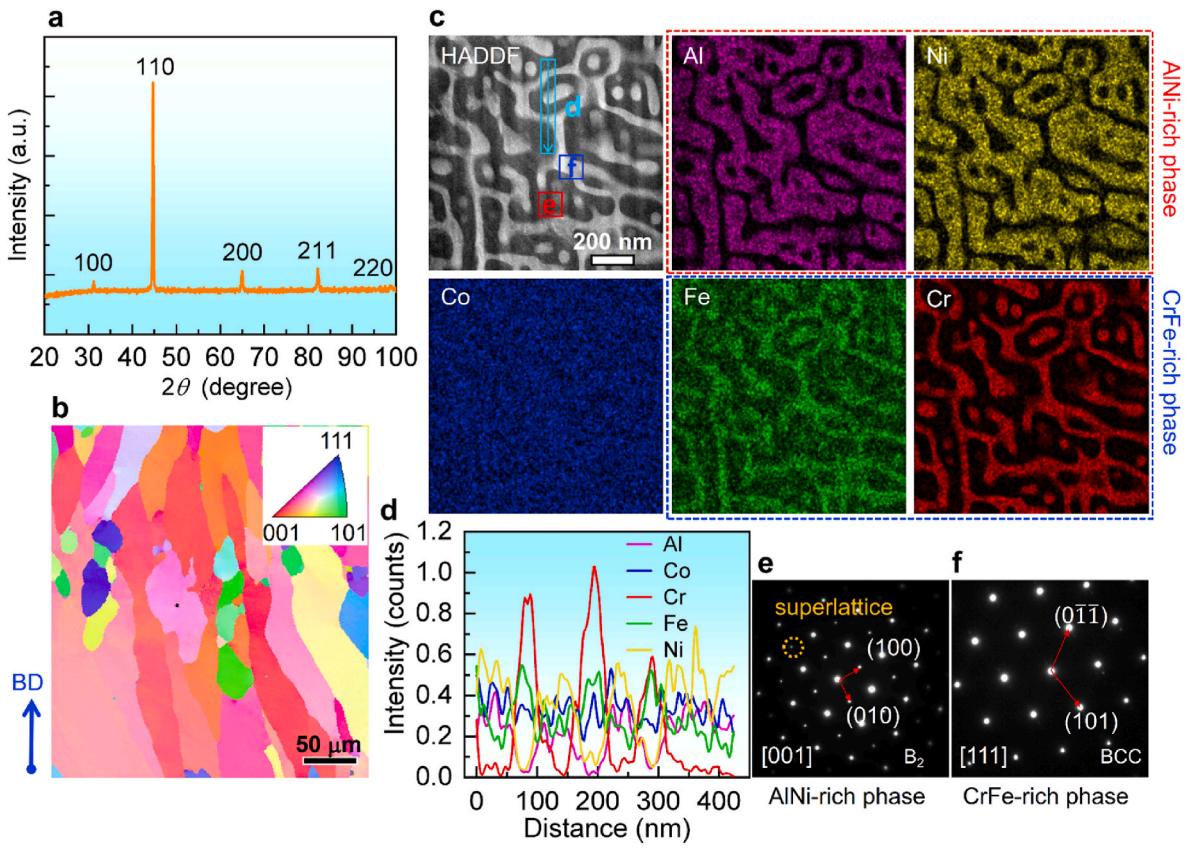

Fig. 1. Microstructure of the as-printed HEA. **a** XRD pattern. **b** Inverse pole figure (IPF) image parallel to the building direction on cross section. **c** Scanning TEM image with EDS mappings showing the duplex BCC phases. **d** Compositional profiles after line scanning of a local region marked by the light blue arrow in **c. e, f** Scanning area electron diffraction images of the B_2 AlNi-rich phase and solid solution CrFe-rich phase marked in **c**, respectively. (For interpretation of the references to color in this figure legend, the reader is referred to the Web version of this article.)

Z-direction was then changed into free boundary and set as shock direction. An atomic layer with thickness of ~1 nm at the bottom was selected as a piston and initially assigned a shock velocity of $U_p = 1$ km/s. The time step for numerical integration of the Newtonian equation of motion is 1 fs for the shock simulations. Atomic configuration was visualized by OVITO software [42]. The local crystalline structure types of atoms were identified by the Polyhedral Template Matching (PTM) algorithm [43] with a cutoff in root-mean-square deviation (RMSD) of 0.15.

3. Results

3.1. Microstructure of the additively manufactured HEA

Fig. 1 displays the typical microstructure of the printed HEA. As can be seen in Fig. 1a, the XRD pattern shows that there are only significant diffraction peaks corresponding to BCC lattice. The EBSD IPF map of Fig. 1b shows that the additively manufactured HEA exhibits obvious [001] fiber texture, and columnar grains spread everywhere in the sample. The width and length of the grains are ~50 μm and ~200 μm, respectively. In Fig. 1c, a detailed TEM observation is also conducted to further characterize the microstructure. The high-angle annular dark-field (HAADF) image illustrates that this additive manufactured HEA is of duplex BCC phases rather than a single BCC solid solution, verified by the noticeable black-white contrast pattern. The corresponding EDS mappings show that the duplex phases are AlNi-rich phase marked by the red dashed rectangular and CrFe-rich phase marked by the blue dashed rectangular, respectively. However, Co element is evenly distributed without any obvious spatial segregation. Such observations also can be validated by a line scanning. Fig. 1d shows the element spatial fluctuation from line scanning marked by the light blue arrow in Fig. 1c. Clearly, the profiles of Al and Ni fluctuate synchronously whereas those of Fe and Cr vary in the same pace. The profile of Co remains fluctuating across the scanned region. According to the period of the profile fluctuation, one can judge that the dimensions of the two phases are both of ~80 nm. Finally, the selected area electron diffraction (SAED) images of the AlNi-rich phase and CrFe-rich phase are displayed in Fig. 1e and f. The diffraction spots suggest the former is an ordered BCC phase (B_2) due to the emergence of the superlattice spots marked by yellow dashed circle. The latter is a chemically disordered BCC phase. Combined with the XRD result, the two phases may differ only elementally but not structurally, so the XRD does not show a visible splitting of the diffraction peaks. According to Fig. 1, the representative characteristics of the as-printed HEA is the columnar grains with [001] texture and duplex BCC structure.

3.2. Reshaped microstructures of the HEA after LSP

After LSP, the additively manufactured HEA exhibits remarkable improved mechanical property. In Fig. 2a, the compressive test curve is illustrated and the work hardening rate is depicted in the inset. It can be observed that when the true strain reaches 0.10, the work hardening rate of the as-printed HEA catastrophically drop, while that of the LSPed HEA still maintain the original trend. Therefore, LSP can significantly prolong the work hardening of the HEA during deformation, enhancing its ultimate strength and uniform elongation, simultaneously. As a result, the uniform compression is increased by 75%, from 12% to 21%. The ultimate compressive strength increased by ~30%, from 2230 MPa to 2900 MPa. In addition, the additively manufactured HEA undergoes significant microstructural evolution from the impact surface to the matrix. On

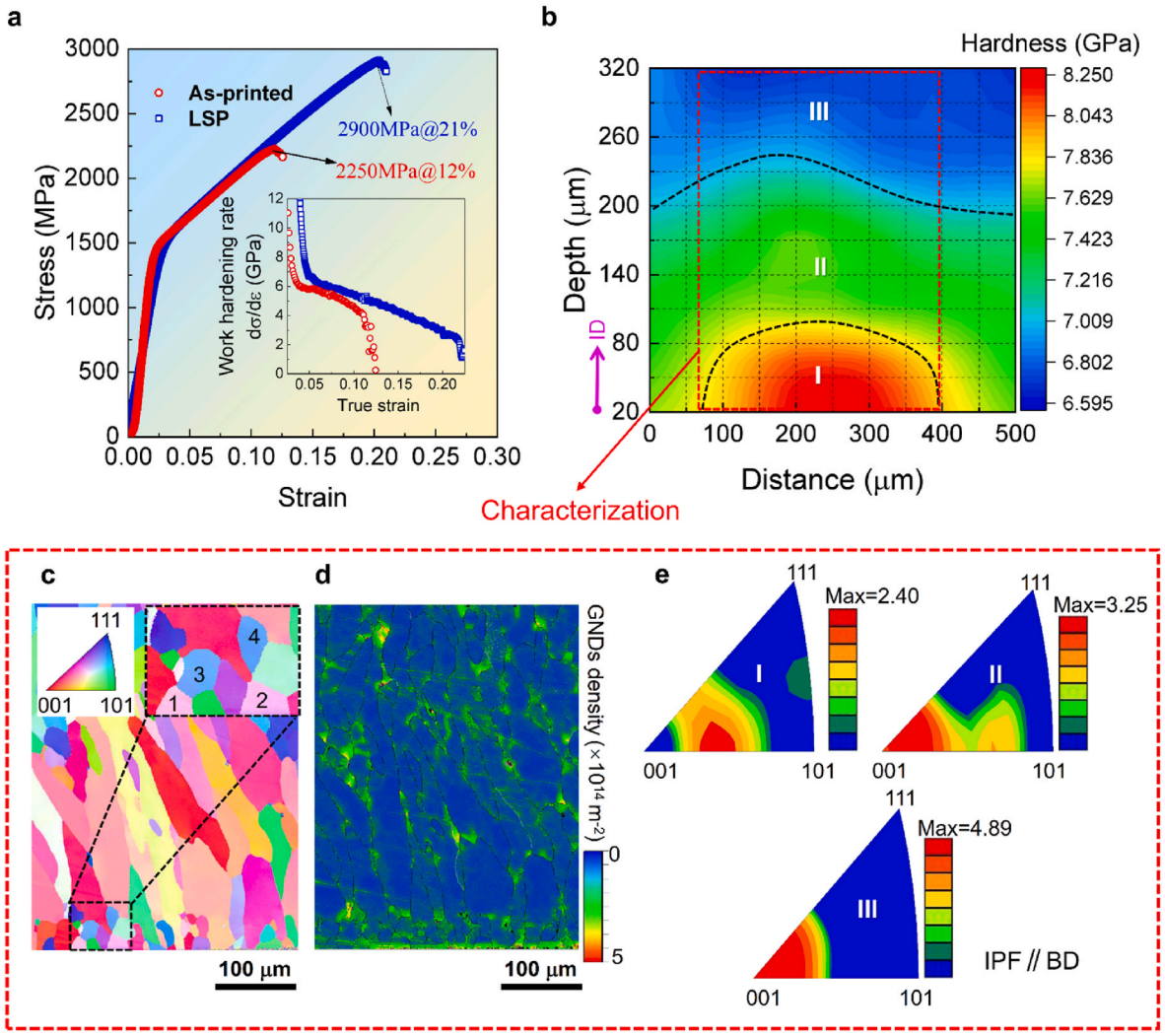

Fig. 2. Mechanical property and morphology of HEA after LSP. **a** Typical compressive engineering stress-strain curves. **b** Spatial distribution of hardness measured by nanoindentation. Three distinct regions appear, i.e., region I, II, III from surface to matrix. The letter 'ID' is short for impact direction. **c** IPF image showing the refined equiaxed grain corresponding to region I. **d** Distribution of the GND density. **e** IPF statistical images from region I to III, which reflect the texture evolution.

the one hand, Fig. 2b presents the shock wave-affected zone along the impact direction (ID), which can be roughly divided into three sections according to the measured magnitude of hardness value. Region I of the outmost region exhibits the highest hardness. In the middle, region II shows a moderate hardness. And consequently region III of the near-substrate zone has the lowest hardness. The thickness of region I is about 100 μm from the LSP surface. Region II is from roughly 100–270 μm. Region III is above 270 μm from the surface. The average hardness of the region I and II are ~8.25 and ~7.42 GPa. Compared with the region III that could be deemed as the LSP unaffected matrix material, these have been increased by about 20% and 10%, respectively. On the other hand, Fig. 2c illustrates that in region I the typical coarse columnar grains have transformed into fine equiaxed grains. The grain refinement zone is about 70 μm from the LSP surface. The refined grains are of a relatively uniform size (~15 μm). More interestingly, these equiaxed grains seem to be regularly and symmetrically distributed on both sides of the parental columnar grain rather than random orientation. The latter is a classical pattern of the refined grains frequently observed in the conventional metallic materials after LSP [44,45]. Further examination implies that the coupled equiaxed grains have the same or approximate orientation, as observed in the grain 1 with 2, and grain 3 with 4; see the enlarged inset of Fig. 2c.

The texture of HEA has been also reshaped remarkably by LSP. In the inner region II and III, the microstructure remains the initial columnar grain morphology. Nonetheless, this does not necessarily mean that the two regions are not affected by the shock wave. On the contrary, direct evidence of the microscopic variation is noticed by spatial distribution of the geometrically necessary dislocations (GNDs). Fig. 2d shows the heat map of GNDs intensity in this alloy after LSP. Visibly, the GNDs density is highest in region I reaching ~3×10^{14} m^{-2} with relative uniform distribution. Seen from surface to interior, it is noticed that GNDs populate on the grain boundaries (GBs) of either larger columnar grains or fine equiaxed grains. A higher GNDs density is presented at GBs while less GNDs density inside grains. This suggests that although the shock wave energy is not sufficient to cause strong grain refinement in region II and III, it still dissipates energy through generating dislocations at GBs. The morphology changes from surface to interior reflect the temporal evolution of surface microstructure during LSP. As for the textural evolution, the local IPF with statistical information is provided in Fig. 2e. Parallel to the BD, the columnar grains in region III (near-substrate zone) exhibit mainly the [001] fiber texture, which is consistent with the result shown in Fig. 1b. In region II, although the main texture is still [001] crystallographic direction, it exhibits a tendency to rotate from [001] to [101]. Furthermore, the texture is between [001] and [101] in region I. This feature further demonstrates that the equiaxed grains are not randomly distributed, which coincides with the findings

in Fig. 2c. According to the texture evolution of the three regions from impact surface to matrix, it is suggested that the initial columnar grains tend to rotate from [001] to [101] direction under the LSP induced shock wave, which will be fragmented into smaller equiaxed grains.

3.3. Atomic observation by TEM and HRTEM

To figure out the atomic-scale deformation mechanism of HEA under LSP, we conduct TEM and HRTEM characterizations to explore the dynamic response of microstructure to the shock wave. In particular, the images of the equiaxed grains near the impact surface are provided in Fig. 3. Compared with the other two inner regions, the shocked surface region contains profuse deformation characteristics due to the strong interactive response to laser shocking. It is easy to see that plenty of unidirectional nanotwins in Fig. 3a and numerous stacking faults (SFs) in Fig. 3b, which all exist near the GBs, can be confirmed by HRTEM observations in Fig. 3c and d. Fig. 3c depicts a typical symmetric lattice arrangement and the conjugate diffraction spots, which are representative features of deformation twinning. Fig. 3d illustrates a typical misfit lattice arrangement and dragging of diffraction spots, which are signal for SFs. Twinning as a medium for plastic deformation is a common phenomenon in BCC metallic materials under extreme deformation conditions such as high stress, high strain rate and low temperature [46–49]. Due to an ultrahigh strain rate produced by LSP, nanotwins and SFs may be easily generated during deformation. However, the size and density of nanotwins produced in this additively manufactured HEA are much lower than those in the conventional counterparts under the same conditions. In HEAs with strong chemical heterogeneity, the local mechanical property always fluctuates from one place to another. This will significantly confine the extension of crystalline imperfections [50], thereby yielding confined volume nanotwins and SFs. In contrast, the planar defects are much extended in the conventional metals and alloys. Moreover, in the latter there often produces multi-directional twinning intersections to segment the matrix to achieve refinement of geometry [32,51].

Another interesting feature is the morphology and spatial distribution of dislocations in the equiaxed grains. From Fig. 3e it is noticed that dislocation density gradually decreases from the GBs to the grain interior, exhibiting a distinct gradient distribution. Significantly, the dislocation density is of the highest value near the GBs, containing only dislocation lines and dislocation tangles but without dislocation walls or dislocation cells. The dislocation lines and tangles are significantly reduced as one moves further away from the GBs, and consequently there is almost no dislocation in any form at the grain center. These observations demonstrate that the critical role of GBs dislocation nucleation and slip in the birth of finer equiaxed grains from the columnar coarse grains. Further, the HRTEM images in Fig. 3f clearly present the spatial nature of dislocations in the equiaxed grains, from GBs to the interior. There is rare report on the gradient distribution of dislocations in the refined grains by LSP. The usual scenario is a gradient distribution of dislocation density along the impact depth, whereas within a single refined grains the dislocation distribution is generally homogeneous, exhibiting high dislocation density and complex dislocation structures [44,51–53]. Thus, we think this is a novel mechanism of grain refinement at the surface of the HEA.

3.4. Atomistic mechanism from computer simulations

The dislocation facilitated grain refinement mechanism under shock loading can be informed by atomistic simulations. Due to the unique structure of the duplex BCC phase, the additively manufactured HEA may exhibit different mechanical properties and structural evolution

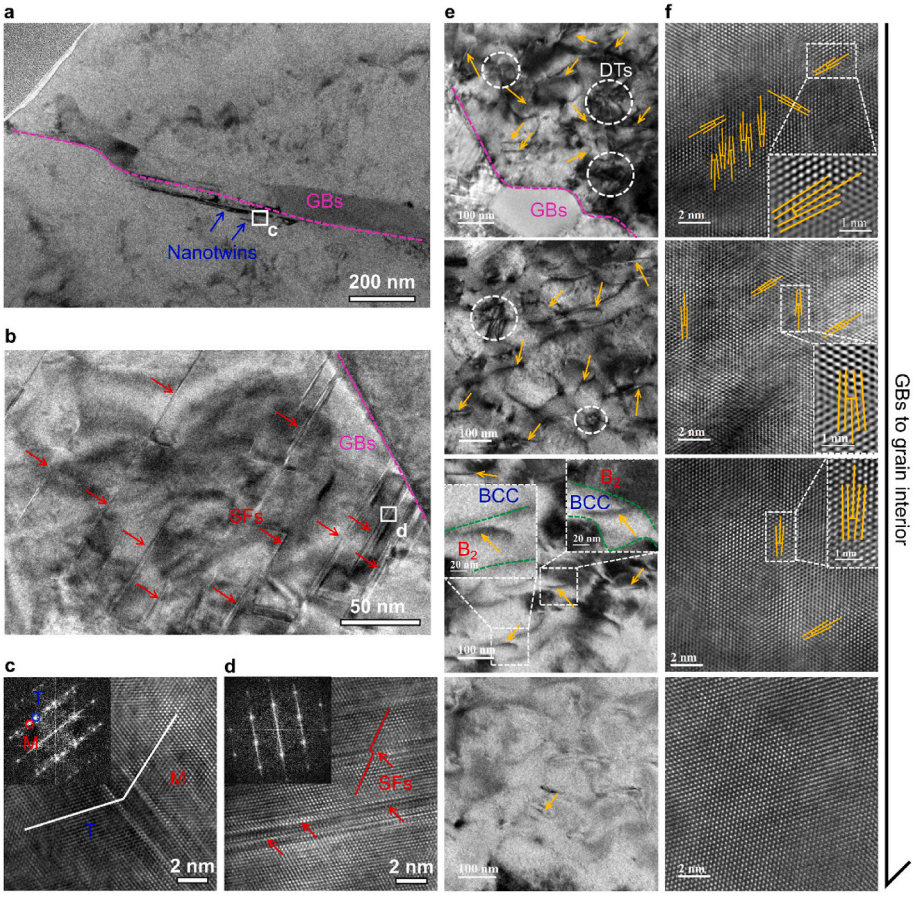

Fig. 3. Surface strengthening mechanism induced by LSP is revealed by TEM and HRTEM. **a** Deformation nanotwins after laser surface treatment. The locations of nanotwins are indicated by the blue arrows. **b** Multiple stacking faults indicated by the red arrows. Nanotwins and stacking faults populate at grain boundaries. **c** Enlarged HRTEM image of a nanotwin and **d** the stacking faults. Insets in **c, d** show the corresponding SEAD of twins and stacking faults, respectively. **e** Gradual decrease of dislocation density from grain boundary to grain interior, in analogy to the trend from surface to matrix. Dislocations are marked by yellow arrows. **f** HRTEM characterization of dislocations corresponding to the locations shown in **e**. (For interpretation of the references to color in this figure legend, the reader is referred to the Web version of this article.)

from those of the conventional alloys under shock loading. However, the real-time mechanical and structural information during the LSP process cannot be obtained directly in experiments due to the technical difficulty in high temporal resolution characterization. Thus, MD simulations were carried out here to reveal detailed structural evolution of HEA. Fig. 4a and b shows the cross section and the front view of the atomic configuration prior to shock. The corresponding atomic structures are also visualized. The dimension of sample is about ~40 nm × 40 nm × 80 nm, containing a total number of 10,465,883 atoms. Two phases (BCC and B_2) are in contact with each other and closely distributed with the same axial direction of the columnar crystallites. The initial structures of both phases are identified as BCC lattice marked as blue atoms. This is because both phases have the same geometric topology in the BCC lattice. The white atoms identified as other structure type belong to the grain boundary. The red atoms at the bottom are set as a piston, as shown in Fig. 4b. This frozen region is used to generate the shock wave by assigning an initial velocity along the shock direction.

The shock wave is generated by driving the piston. As the piston moves upwards along Z direction, the region adjacent to the piston will move at the same speed and cause the atoms in the vicinity to gather more tightly. Thus, shock leads to an increase in local mass density. Meanwhile, the resultant density further pushes the near-adjacent atoms, therefore, making the shock wave propagate at a faster speed denoted as U_s. The shock speed can be determined by measuring the propagation of shock front in the sample at various time. Fig. 4c shows the distribution of the averaged Z-component velocity from 1 ps to 10 ps with a time interval of 1 ps. As shock continues, more and more regions move upwards. The averaged Z-component velocity increases from zero at the position where the front of the shock wave arrives, which is ahead of the position of piston. The spatial distribution of dislocation density also shows a similar trend, as shown in Fig. 4d. At about 10 ps, the uppermost region has an upward velocity, indicating the shock wave has reached the upper surface. Fig. 4e presents visualizations of the atomic shear strain during shock process. Dislocations are mainly nucleated from the GBs, which is consistent with the experimental observation of high dislocation density at GBs in Fig. 3. Within 10 ps (the above graphs), the length of sample becomes shorter and shorter as the upper region remains stationary. A special pattern of atomic strain distribution can be observed. In each columnar grain, localized strains extend in different directions due to the random orientation of crystallites and terminate at grain boundaries. This pattern of strains also spread upwards as the shock wave propagates towards the upper surface. Once the shock wave reached the upper surface after 10 ps (the bottom graphs), a new wave was formed and reflected into the sample, making the sample in a tensile state. As can be seen, the length of sample increases from 12 ps to 35 ps. Moreover, the strain distribution in B_2–AlNi crystals is more heterogeneous than that of BCC-FeCr crystals, which eventually suffers extreme plasticity locally and develops cavities. The structural evolutions after the reflection of the shock wave, as shown in Fig. 4f, indicate that atomic amorphizations at strain concentration in the biphasic columnar crystals lead to some fine grains near the bottom of sample. The amorphization is caused by the multiple dislocation slip in the same slip plane, which will transform to grain boundary in the new fine grains. At the same time, FCC and HCP phases were also precipitated in the BCC-FeCr crystals. As both phases are forced to deform simultaneously with same strain in simulations, the phase transitions in BCC-FeCr crystals can compensate the strain compared with the part induced by the extreme plasticity in B_2–AlNi. Therefore, the strain distribution in BCC-FeCr crystals was more homogeneous than that in B2–AlNi crystals as subjected to a large tensile strain. However, it is difficult to observe in experiments as two phases can be deformed in different strains. In addition, the shock wave can be dissipated during the propagating in experiments, thus GND density diagram in Fig. 2d shows no obvious difference between two phases.

Our simulations reveal the mechanical properties of duplex BCC columnar crystals under shock loading, which is rarely reported in the literature [54,55]. The HEA sample exhibit a special pattern of atomic strain distribution due to the columnar crystal structure which evolves with the shock process. Both phases behave similarly during the shock compression as no significant phase transformation occurs. Considering the temporal and spatial limitations of MD simulations and the reliability of current empirical potential, the model sample constructed and the applied shock loading in the simulations are not identical to the experimental conditions. Although MD simulations allows to observe the process of grain refinement through repeated dislocation slip and amorphization, grain rotation is hard to observe due to the diffusive nature of grain boundary mobility that requires much longer time scale to survey, which is much beyond the timescale window of classical

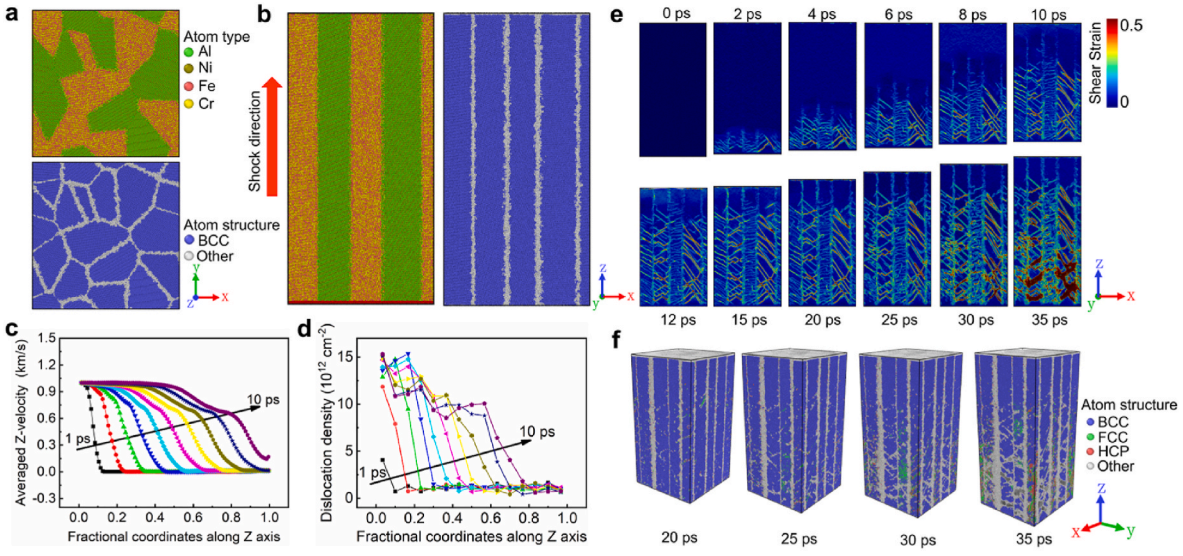

Fig. 4. Atomistic simulations of the shock mechanism in the duplex BCC polycrystalline HEA. **a** Atomic configuration of the polycrystalline model viewed from cross section. B_2 and BCC grains are alternatively distributed. In the upper panel, atoms are colored by elements while in the bottom panel crystallites and grain boundary are recognized by the polyhedral template matching method. **b** Front view of the sample. The coloring scheme is identical to **a**. **c, d** Velocity and dislocation density profiles along the shocking direction. **e** Evolution of atomic shear strain during shock. **f** Operation of the transient unstable dislocations amid shocking process of the dual-phase HEA sample.

molecular dynamics.

4. Discussion

4.1. Deformation mechanism

When the shock wave pressure exceeding Hugoniot elastic limit enters the conventional alloys, it will cause severe plastic deformation, resulting in huge microstructural evolution to dissipate shock energy. This process usually produces extremely high density dislocations [44,52], generates multi-directional deformation twinning [32,45,51] or shear bands [56], and induces phase transition [29], etc. The deformation mechanism found here is different from those existing in conventional alloys. First, dislocation density exhibits obvious gradient distribution from GBs to interior. The overall dislocation density is low and dislocation morphology is simple in the form of dislocation lines and a small number of dislocation tangles. It suggests that these dislocations are not statistically stored dislocations but GNDs. The latter only serves to maintain the strain gradient induced by the possible inhomogeneous deformation. Next, the unidirectional nanotwins and many SFs are simultaneously observed near the GBs. The reason for the dislocation features is probably ascribed to the unique structural characteristics of this HEA. Compared with conventional alloys, this HEA has severe lattice distortion, which will significantly suppress the nucleation of dislocations and impede the mobility of existing dislocations. Consequently, the crystalline imperfections have more probability to be confined in a local region with severe lattice resistance that provided by chemical short-range order [57]. Then, LSP allows for un ultrahigh strain rate up to $\sim 10^7$/s. Under this extreme condition, deformation twins and SFs are easy to generate as a medium for plastic deformation. Nanotwins and high density SFs also hinders the movement of dislocations. Finally, this HEA are of duplex BCC phases. Dislocations generated in one phase tend to end at the phase boundary, as shown in Fig. 3e (third panel from top). For instance, the dislocation lines nucleated at one B_2/BCC phase boundary tend to penetrate the other BCC/B_2 phase boundary but unfortunately terminate at the interface. All these factors lead to the low concentration and simple morphology of dislocations in this unique HEA by additive manufacturing.

4.2. Theoretical model for grain rotation

The mechanism of grain refinement under LSP in conventional metals is often attributed to dynamic recrystallization (DRX) [51,52,56]. However, the existing DRX mechanism cannot explain the experimental findings in this additively manufactured HEA. For conventional DRX, the newly formed grains often exhibit gradient distribution from nanograin to micrograin along the impact depth. In addition, due to dislocation evolution without tendency, the newly formed grains are generally randomly orientated without any texture. Meanwhile, the density of dislocations at the same impact depth is the same, so dislocations within grains at the same depth tend to be uniformly distributed. The structural characteristics of the equiaxed grains in this present HEA are unique: (1) strong tendency of texture evolution from [001] to [101] crystallographic direction; (2) the symmetrical distribution of refined grains around their parental columnar grain bounds; (3) similar size and no gradient structure; (4) no complex dislocation morphology generated within the equiaxed grains but leaving nanotwins, SFs near GBs. To understand and explain these characteristics, a rotation mechanism of columnar grains is proposed to interpret the grain refinement. Due to the newly formed grains appear certain symmetry and are closely related to the GNDs, the grain refinement mechanism in our work may be similar to the lattice curvature induced-grain fragmentation model proposed by Laszlo S. Toth et al. [58]. The basic assumption is that lattice rotation within an individual grain is impeded near the GBs by the constraining effects of the neighboring grains during deformation, which gives rise to lattice curvature. The lattice curvature is generated along with the GNDs. When the curvature is enough large, a new grain will be formed. However, in Ref. [58], the target parent grains are equiaxed grains rather than the representative columnar grains in this work. Given the noticeable anisotropic of columnar grains, an amended lattice curvature mechanism of columnar grains is proposed to interpret the grain refinement.

Fig. 5a depicts a schematic of the lattice rotation in columnar grains accommodated by dislocation slip, which could be used to understand the grain refinement in the HEA after LSP (Notice, in Fig. 5a, a semi-ellipse is selected as the geometric model for the columnar grain rather than a full ellipse. This is because the columnar grains of which grain refinement occurs are almost entirely on or near the impact surface. Therefore, these grains may have already been destroyed due to the mechanical grinding and polishing before LSP.). Due to the ultra-high strain rate near the impact surface, the columnar grains will undergo severe plastic deformation in the form of lattice rotation driven by dislocations, nanotwins and SFs. This mechanism has been partially verified by the atomistic simulations. However, owing to the constraint from neighboring grains, plastic deformation is inhomogeneous and the rotation of the crystallographic plane near the GBs is smaller than that in the middle of the grains. This will results in mismatch between the middle part and the near-GBs zone [58]. In other words, the columnar grain could be divided into two sections, i.e., the rotated zone marked by purple color and the constrained zone marked by blue color. The rotated crystallographic plane would be curved within periphery part near the GBs owing to confinement, resulting in mismatch between the distorted plane and the undistorted plane. GNDs are necessary to coordinate the inhomogeneous deformation. As plastic deformation gradually increases, the distorted plane can no longer maintain continuous with the undistorted part and therefore, independent equiaxed grain (marked by hexagon in Fig. 5a) will be produced at the periphery part near the parental columnar grain boundaries.

As mentioned above, GNDs must be generated to accommodate the inhomogeneous deformation during the formation of equiaxed grains. According to [58], GNDs density can be expressed as:

$$\rho_{\mathrm{GNDs}} = \frac{\kappa}{b} \tag{1}$$

where $\kappa = 1/\mathrm{r}$ represents the curvature of the distorted plane, r represents the radius of curvature, and b is the magnitude of the Burgers vector. For arbitrary distorted plane, r can be obtained from the geometry illustrated in Fig. 5b. As can be seen, the relative rotation angle θ between rotated zone and constrained zone would lead to an average misorientation Ω between undistorted plane and distorted plane. When Ω is sufficiently large, an independent grain would be formed in principle. Hence, the Ω can be regarded as the GBs angle between the equiaxed grains and their parental columnar grains. The Ω and r depends on the θ, which can be expressed as:

$$\sin\Omega_{1,2} = \sqrt{\frac{(1-\cos\theta)\left[\gamma^2(1-\xi^2)(1+\cos\theta) \pm 2\gamma\xi\sin\theta\sqrt{1-\xi^2} + \xi^2(1-\cos\theta)\right]}{\gamma^2\left(1+\beta^2-2\xi^2-2\cos\theta\sqrt{1-\xi^2}\sqrt{\beta^2-\xi^2}\right) \pm 2\gamma\xi\sin\theta\left(\sqrt{1-\xi^2}-\sqrt{\beta^2-\xi^2}\right)+2\xi^2(1-\cos\theta)}} \tag{2}$$

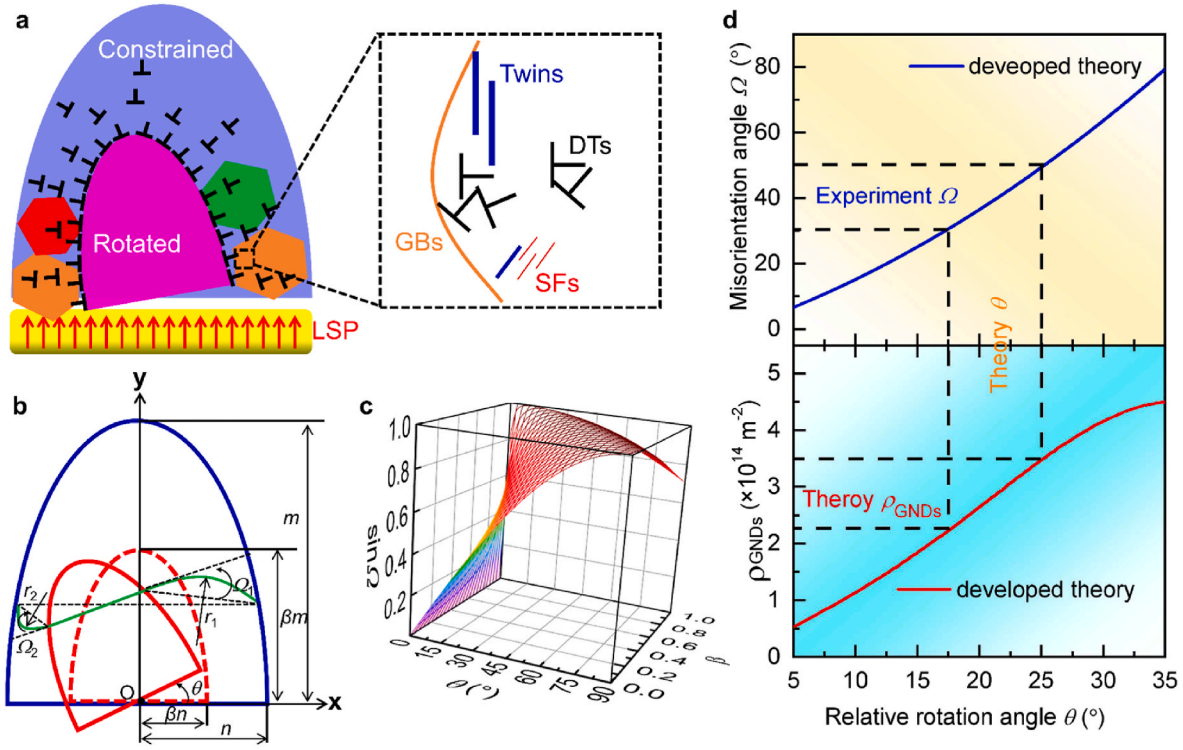

Fig. 5. Theoretical model for the columnar grain rotation. **a** Schematic of the dynamic rotation and subsequent refinement of the columnar grains during LSP. Enlarged view showing plastic flow primitives that assist grain rotation. **b** Graphics for calculating the misorientation Ω and GNDs density due to the lattice plane distortion near the GBs. **c** Relationship of relative rotation angle θ and rotation-factor β to misorientation Ω. d Theory of the relationships of Ω-θ and ρ_{GNDs}-θ under $\beta = 1/3$ of the columnar grain. Theory is in agreement with the experimental results, where experimental value of Ω can be obtained from IPF.

and

$$r_{1,2}=\frac{2\sqrt{(1-\cos\theta)\left[\gamma^2(1-\xi^2)(1+\cos\theta)\pm 2\gamma\xi\sin\theta\sqrt{1-\xi^2}+\xi^2(1-\cos\theta)\right]}}{m\left[\gamma^2\left(1+\beta^2-2\xi^2-2\cos\theta\sqrt{1-\xi^2}\sqrt{\beta^2-\xi^2}\right)\pm 2\gamma\xi\sin\theta\left(\sqrt{1-\xi^2}-\sqrt{\beta^2-\xi^2}\right)+2\xi^2(1-\cos\theta)\right]} \tag{3}$$

where β is defined as a rotation-factor to quantify the volume of the rotated zone. $\gamma = n/m$, n and m is the width and length of the columnar grain. $\xi = y_0/m$ ($\xi \le \beta$) represents the position of the characteristics lattice plane. And, therefore,

$$\rho_{GNDs_{1,2}}=\frac{2\sqrt{(1-\cos\theta)\left[\gamma^2(1-\xi^2)(1+\cos\theta)\pm 2\gamma\xi\sin\theta\sqrt{1-\xi^2}+\xi^2(1-\cos\theta)\right]}}{bm\left[\gamma^2\left(1+\beta^2-2\xi^2-2\cos\theta\sqrt{1-\xi^2}\sqrt{\beta^2-\xi^2}\right)\pm 2\gamma\xi\sin\theta\left(\sqrt{1-\xi^2}-\sqrt{\beta^2-\xi^2}\right)+2\xi^2(1-\cos\theta)\right]} \tag{4}$$

Fig. 5c depicts the relationship of θ and β to Ω. For convenience, we use sinΩ to represent its change. As mentioned above, when Ω is large enough, an independent equiaxed grain will be formed, that is, the faster the Ω increases, the more prone to columnar grains fragmented to equiaxed grains. Significantly, the larger the β, the faster the increase of sinΩ under the same θ. This means that the grain refinement of the columnar grains is very sensitive to the volume of the rotated zone. The larger the β, the larger the rotated zone, and thus more severe the distorted plane. Consequently, it is easier to form equiaxed grain.

In this work, the equiaxed grain size is ~15 μm (Fig. 2c) and thus β is estimated as ~1/3 according to Fig. 5b. The theoretical relationship curves of Ω-θ and ρ_{GNDs}-θ under $\beta = 1/3$ is provided in Fig. 5d. It can be observed that as the relative rotation angle θ increases, both Ω and ρ_{GND} increase gradually. In this work, the interval of the Ω value is about 30°–50°, as can been in Fig. A1. Its corresponding theoretical θ is about 17.5°–25.0°. With this θ interval, the theoretical density of GNDs is ~2.3–3.5 $\times 10^{14}$ m^{-2}. This scope is very consistent with the experimental result ~3×10^{14} m^{-2} (Fig. 2d). Therefore, the developed rotation model of columnar grains is efficacious.

The proposed rotation mechanism for columnar grains can explain

the four findings in experiments that differs from the mechanism of the conventional DRX.

(1) Since the equiaxed grains are induced by θ between the rotated zone and the constrained zone, the orientations of the equiaxed grain are directional rather than random (Fig. 2c).
(2) Due to the distorted crystallographic plane symmetrically distributed at the constrained zone near the GBs, the equiaxed grains with the same or approximate orientations are symmetrically distributed near the parental columnar grain boundaries (Fig. 2c).
(3) The size of the equiaxed grains depends on the rotation factor β, which directly leads to the size of equiaxed grains to be of the same order of magnitude as that of parental columnar grains. Therefore, the equiaxed grain size is relatively uniform. There will be no gradient distribution from nanoscale grains to microscale grains.
(4) Since grain refinement is resulted from lattice rotation in columnar grains through nucleation and motion of dislocations, nanotwins and SFs is prevalent rather than the homogeneous complex dislocation structures in the equiaxed grains. The latter is a scenario for the common DRX mechanism. On the contrary, the dislocations in the form of GNDs exhibit significant gradient distribution from GBs to interior, which supplies the inhomogeneous deformation by rotation of the columnar grain.

4.3. Explanation of the improved mechanical property

After LSP treatment, the mechanical performance of the HEA has been improved. This is due to the grain refinement in region I, forming a sandwich-like structure, i.e., the coarse columnar grains in the core and the fine equiaxed grains on the surface layer. During deformation, the inner columnar grains will yield preferentially and then gradually transition to the outer equiaxed grains. Theoretically, since the equiaxed grains region is a hard layer compared with the columnar coarse grains, the overall yield strength should be improved based on a rule-of-mixture. However, the grain refinement region is too small, only about 70 μm as can be seen in Fig. 2c. Even though these equiaxed grains would microscopically produce a strengthening effect, the macroscopic yield strength of the HEA exhibits hardly any difference before and after LSP, as can be seen in Fig. 2a.

Although a very thin layer of equiaxed grains may not effectively delay the HEA yielding, it can significantly delay fracture. This is indicated by the noticeable enhancement of ductility and ultimate strength in Fig. 2a. Wang et al. [59] reported the detailed necking analysis of hard-film-on-soft-substrate structures (e.g., gradient or sandwich structures just like the hard equiaxed grains layer-on-soft columnar grains core in this work). They pointed out that for such a heterogeneous structure, the outer hard layer (even for a very thin layer) is the key to controlling overall uniform ductility, rather than the Considère condition of the soft core. Inspired by this, it can assume that the equiaxed grains layer would significantly delay the overall fracture and thus increase ductility and ultimate strength.

In the future, an urgent task is to optimize the LSP parameters that will increase the area of grain refinement region. This may lead to a synergy increase in yield strength and ductility, becoming a promising strategy of strength-ductility trade-off overcome.

5. Conclusion

To summarize, we propose to use LSP to process a category of dual-phase AlCoCrFeNi high-entropy alloys which have been fabricated by additive manufacturing. This strategy enables to significantly reshape the morphology of HEA at the impact surface and improve mechanical performance. The grain refinement is achieved via novel mechanism of lattice rotation in the parental columnar coarse grain. This mechanism is different from the existing DRX mechanism, the typical imperfection morphology of which is the homogeneous spatial distribution of dislocations. Here we observe conspicuous gradient about the GNDs density from the new-born grain boundary to the grain interior. This suggests a significant role of GNDs nucleation in facilitating the refined equiaxed grain rotation. The mechanism of grain refinement can be partially verified by large-scale molecular dynamics simulations of shock loading on HEA, which finds abundant dislocations at the shock surface. The dislocations are mainly nucleated from GBs and experience significant slip along the same slip plane. Multiple slip of unstable dislocations on the same slip plane finally causes local amorphization, which serves as GBs of the small new grains born in the parental smaller grains. We attribute the novel deformation phenomena to the unique structural feature of the additively manufactured HEA – dual phase B_2 + BCC and strong local mechanical fluctuation – that geometrically confines crystalline defect. The novel grain refinement mechanism is further rationalized by a continuum-level model, which predicts that GNDs should be generated to coordinate the plastic deformation of grain rotation and thus, the dislocation density exhibits a gradient distribution. The present work combining structural characterization, atomistic simulations, and theoretical model provides fundamental insights into bottom-up approach to enhance the mechanical performance of the recently advanced multi-principal-element alloys based on morphology decoration via LSP.

CRediT authorship contribution statement

Yunjian Bai: Conceptualization, Methodology, Investigation, Validation, Writing – original draft, Writing – review & editing. **Guo-Jian Lyu:** Conceptualization, Methodology, Investigation, Validation, Writing – original draft, Writing – review & editing. **Yun-Jiang Wang:** Investigation, Validation, Methodology, Writing – review & editing. **Tianyu Chen:** Methodology, Validation, Writing – review & editing. **Kun Zhang:** Conceptualization, Methodology, Validation, Supervision, Resources, Project administration, Writing – review & editing. **Bingchen Wei:** Conceptualization, Methodology, Validation, Supervision, Funding acquisition, Project administration, Writing – review & editing.

Declaration of competing interest

The authors declare that they have no known competing financial interests or personal relationships that could have appeared to influence the work reported in this paper.

Data availability

Data will be made available on request.

Acknowledgment

This work was supported by the National Natural Science Foundation of China (Grant No. 12272392, No. 11790292), the Strategic Priority Research Program of the Chinese Academy of Sciences (Grant No. XDB22040303), and the Innovation Program (237099000000170004). YJW acknowledges the financial support from the NSFC (Grant No. 12072344) and the Youth Innovation Promotion Association of the Chinese Academy of Sciences.

Appendix

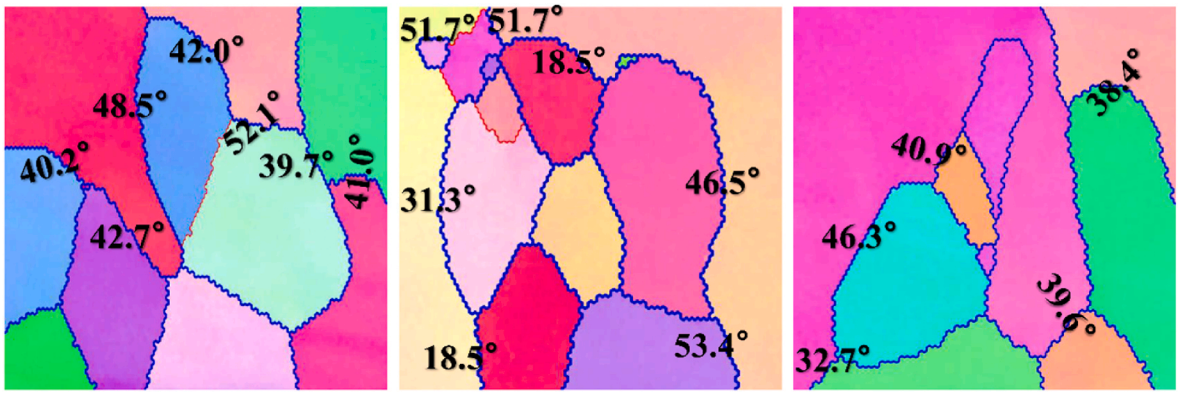

Fig. A1. Misorientation Ω between the equiaxed grains and their parent columnar grain.

The derivation process of sin Ω and ρ_{GNDs} is given as following.

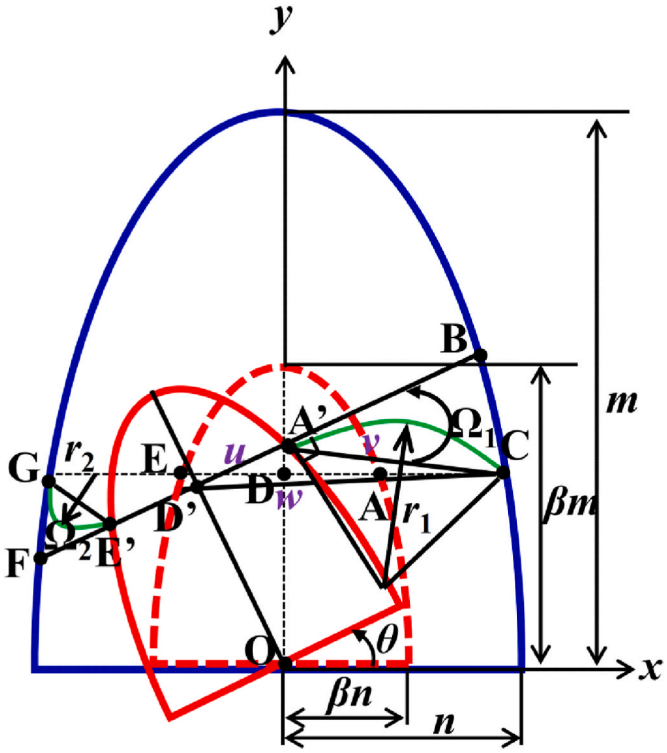

Fig. A2. The graphics for calculating the misorientation Ω and *GNDs* density.

Seen from Fig. A2, a columnar grain is regarded as a large ellipse (blue line), and the freely rotating part is regarded as a small ellipse (red line) that is scaled down. For arbitrary specific crystallographic plane, point A (x_0, y_0) is on the contour of the small ellipse, point D $(0, y_0)$ is inside the small ellipse, and point C (x_1, y_0) is on the contour of the large ellipse. Therefore, A and C satisfy their corresponding elliptic equation, respectively, i.e.,

$$\frac{x_0^2}{\beta^2 n^2} + \frac{y_0^2}{\beta^2 m^2} = 1 \tag{A1}$$

$$\frac{x_1^2}{n^2} + \frac{y_0^2}{m^2} = 1 \tag{A2}$$

For the sake of simplicity, we only illustrate the rotation of the small ellipse relative to the large ellipse, while ignoring the synchronous rotation of the two ellipses. Due to different rotation capabilities, the small ellipse is rotated by θ relative to the large ellipse and, therefore, point A will rotate to A′, point D will rotate to D' while point C is still in the original position. A' $(x_{A'}, y_{A'})$ and D' $(x_{D'}, y_{D'})$ can be determined:

$$\begin{pmatrix} x_{A'} \\ y_{A'} \end{pmatrix} = \begin{pmatrix} \cos\theta & -\sin\theta \\ \sin\theta & \cos\theta \end{pmatrix} \cdot \begin{pmatrix} x_0 \\ y_0 \end{pmatrix} = \begin{pmatrix} x_0\cos\theta - y_0\sin\theta \\ x_0\sin\theta + y_0\cos\theta \end{pmatrix} \tag{A3}$$

$$\begin{pmatrix} x_{D'} \\ y_{D'} \end{pmatrix} = \begin{pmatrix} \cos\theta & -\sin\theta \\ \sin\theta & \cos\theta \end{pmatrix} \cdot \begin{pmatrix} 0 \\ y_0 \end{pmatrix} = \begin{pmatrix} -y_0 \sin\theta \\ y_0 \cos\theta \end{pmatrix} \tag{A4}$$

Therefore, the u, v and w can be determined and subsequent sin Ω1 can be expressed as following:

$$\sin\Omega_1 = \sqrt{1 - \left(\frac{u^2+v^2-w^2}{2uv}\right)^2} = \sqrt{\frac{(1-\cos\theta)(x_1^2\cos\theta - y_0^2\cos\theta + x_1^2 + y_0^2 + 2x_1y_0\sin\theta)}{x_0^2 - 2y_0^2\cos\theta + x_1^2 + 2y_0^2 - 2x_0x_1\cos\theta - 2x_0y_0\sin\theta + 2x_1y_0\sin\theta}} \tag{A5}$$

According to Eqs. (A1) and (A2), x_0 and x_1 can be expressed as following, respectively:

$$x_0 = \beta n\sqrt{\left(1 - \frac{y_0^2}{\beta^2 m^2}\right)} \tag{A6}$$

$$x_1 = n\sqrt{\left(1 - \frac{y_0^2}{m^2}\right)} \tag{A7}$$

In addition, we define:

$$\gamma = \frac{n}{m} \tag{A8}$$

$$\xi = \frac{y_0}{m} \quad (\xi \le \beta) \tag{A9}$$

Therefore, Eq. (A5) can be further organized as following:

$$sin\ \Omega_1 = \sqrt{\frac{(1-cos\ \theta)(x_1^2\ cos\ \theta + x_1^2)}{x_0^2 + x_1^2 - 2x_0x_1\ cos\ \theta}} = \frac{sin\ \theta}{\sqrt{(\beta^2 - 2\beta\ cos\ \theta + 1)}}, y_0 = 0 \tag{A10}$$

$$\begin{aligned}
\sin\Omega_1 &= \sqrt{\frac{(1-\cos\theta)\left(\frac{n^2}{m^2}\frac{(m^2-y_0^2)}{y_0^2}\cos\theta - \cos\theta + \frac{n^2}{m^2}\frac{(m^2-y_0^2)}{y_0^2} + 1 + 2\frac{n}{m}\frac{\sqrt{(m^2-y_0^2)}}{y_0}\sin\theta\right)}{\frac{n^2}{m^2}\frac{(\beta^2a^2-y_0^2)}{y_0^2} - 2\cos\theta + \frac{n^2}{m^2}\frac{(m^2-y_0^2)}{y_0^2} + 2 - 2\frac{n^2}{m^2}\frac{\sqrt{(\beta^2m^2-y_0^2)(m^2-y_0^2)}}{y_0^2}\cos\theta - 2\frac{n}{m}\frac{\sqrt{(\beta^2m^2-y_0^2)}}{y_0}\sin\theta + 2\frac{n}{m}\frac{\sqrt{(m^2-y_0^2)}}{y_0}\sin\theta}} \\
&= \sqrt{\frac{(1-\cos\theta)\left(\gamma^2\frac{(1-\xi^2)}{\xi^2}\cos\theta - \cos\theta + \gamma^2\frac{(1-\xi^2)}{\xi^2} + 1 + 2\gamma\frac{\sqrt{(1-\xi^2)}}{\xi}\sin\theta\right)}{\gamma^2\frac{(\beta^2-\xi^2)}{\xi^2} - 2\cos\theta + \gamma^2\frac{(1-\xi^2)}{\xi^2} + 2 - 2\gamma^2\frac{\sqrt{(\beta^2-\xi^2)(1-\xi^2)}}{\xi^2}\cos\theta - 2\gamma\frac{\sqrt{(\beta^2-\xi^2)}}{\xi}\sin\theta + 2\gamma\frac{\sqrt{(1-\xi^2)}}{\xi}\sin\theta}} \\
&= \sqrt{\frac{(1-\cos\theta)\left[\gamma^2(1-\xi^2)(1+\cos\theta) + 2\gamma\xi\sin\theta\sqrt{1-\xi^2} + \xi^2(1-\cos\theta)\right]}{\gamma^2\left(1+\beta^2-2\xi^2-2\cos\theta\sqrt{1-\xi^2}\sqrt{\beta^2-\xi^2}\right) + 2\gamma\xi\sin\theta\left(\sqrt{1-\xi^2} - \sqrt{\beta^2-\xi^2}\right) + 2\xi^2(1-\cos\theta)}}, \quad y_0 \ne 0
\end{aligned} \tag{A11}$$

As can be seen, Eqs. (A10) and (A11) can be combined to one:

$$\sin\Omega_1 = \sqrt{\frac{(1-\cos\theta)\left[\gamma^2(1-\xi^2)(1+\cos\theta) + 2\gamma\xi\sin\theta\sqrt{1-\xi^2} + \xi^2(1-\cos\theta)\right]}{\gamma^2\left(1+\beta^2-2\xi^2-2\cos\theta\sqrt{1-\xi^2}\sqrt{\beta^2-\xi^2}\right) + 2\gamma\xi\sin\theta\left(\sqrt{1-\xi^2} - \sqrt{\beta^2-\xi^2}\right) + 2\xi^2(1-\cos\theta)}} \tag{A12}$$

The GNDs density can be expressed as:

$$\rho_{GNDs} = \frac{\kappa}{b} = \frac{1}{rb} \tag{A13}$$

$$r_1 = \frac{v}{2\cos\left(\frac{\pi}{2} - \Omega\right)} = \frac{x_0^2 - 2y_0^2\cos\theta + x_1^2 + 2y_0^2 - 2x_0x_1\cos\theta - 2x_0y_0\sin\theta + 2x_1y_0\sin\theta}{2\sqrt{(1-\cos\theta)(x_1^2\cos\theta - y_0^2\cos\theta + x_1^2 + y_0^2 + 2x_1y_0\sin\theta)}} \tag{A14}$$

where κ and r represents the curvature and radius of curvature, respectively. Bring Eqs. (A6–A9) into Eqs. (A13) and (A14), the ρ_{GNDs} can be derived as following:

$$\rho_{GNDs}^1 = \frac{2\sqrt{(1-\cos\theta)\left[\gamma^2(1-\xi^2)(1+\cos\theta) + 2\gamma\xi\sin\theta\sqrt{1-\xi^2} + \xi^2(1-\cos\theta)\right]}}{bm\gamma^2\left(1+\beta^2-2\xi^2-2\cos\theta\sqrt{1-\xi^2}\sqrt{\beta^2-\xi^2}\right) + 2\gamma\xi\sin\theta\left(\sqrt{1-\xi^2} - \sqrt{\beta^2-\xi^2}\right) + 2\xi^2(1-\cos\theta)} \tag{A15}$$

Analogous, due to the symmetrical relationship between the coordinates of point A and point E, sin Ω_2 and ρ_{GNDs}^2 can be obtained as following:

$$\sin\Omega_2=\sqrt{\frac{(1-\cos\theta)\left[\gamma^2\left(1-\xi^2\right)(1+\cos\theta)-2\gamma\xi\sin\theta\sqrt{1-\xi^2}+\xi^2(1-\cos\theta)\right]}{\gamma^2\left(1+\beta^2-2\xi^2-2\cos\theta\sqrt{1-\xi^2}\sqrt{\beta^2-\xi^2}\right)-2\gamma\xi\sin\theta\left(\sqrt{1-\xi^2}-\sqrt{\beta^2-\xi^2}\right)+2\xi^2(1-\cos\theta)}} \tag{A16}$$

$$\rho_{GNDs}^2=\frac{2\sqrt{(1-\cos\theta)\left[\gamma^2\left(1-\xi^2\right)(1+\cos\theta)-2\gamma\xi\sin\theta\sqrt{1-\xi^2}+\xi^2(1-\cos\theta)\right]}}{bm\gamma^2\left(1+\beta^2-2\xi^2-2\cos\theta\sqrt{1-\xi^2}\sqrt{\beta^2-\xi^2}\right)-2\gamma\xi\sin\theta\left(\sqrt{1-\xi^2}-\sqrt{\beta^2-\xi^2}\right)+2\xi^2(1-\cos\theta)} \tag{A17}$$

References

[1] J.W. Yeh, S.K. Chen, S.J. Lin, J.Y. Gan, T.S. Chin, T.T. Shun, C.H. Tsau, S.Y. Chang, Adv. Eng. Mater. 6 (2004) 299–303+274.
[2] Y. Zhang, T.T. Zuo, Z. Tang, M.C. Gao, K.A. Dahmen, P.K. Liaw, Z.P. Lu, Prog. Mater. Sci. 61 (2014) 1–93.
[3] B. Gludovatz, A. Hohenwarter, D. Catoor, E.H. Chang, E.P. George, R.O. Ritchie, Science 345 (2014) 1153–1158, 84.
[4] Z. Li, K.G. Pradeep, Y. Deng, D. Raabe, C.C. Tasan, Nature 534 (2016) 227–230.
[5] E.P. George, D. Raabe, R.O. Ritchie, Nat. Rev. Mater. 4 (2019).
[6] Q. Ding, Y. Zhang, X. Chen, X. Fu, D. Chen, S. Chen, L. Gu, F. Wei, H. Bei, Y. Gao, M. Wen, J. Li, Z. Zhang, T. Zhu, R.O. Ritchie, Q. Yu, Nature 574 (2019) 223–227.
[7] P. Shi, R. Li, Y. Li, Y. Wen, Y. Zhong, W. Ren, Z. Shen, T. Zheng, J. Peng, X. Liang, P. Hu, N. Min, Y. Zhang, Y. Ren, P.K. Liaw, D. Raabe, Y.D. Wang, Science 373 (2021) 912–918, 84.
[8] M. Naeem, H. He, F. Zhang, H. Huang, S. Harjo, T. Kawasaki, B. Wang, S. Lan, Z. Wu, F. Wang, Y. Wu, Z. Lu, Z. Zhang, C.T. Liu, X.L. Wang, Sci. Adv. 6 (2020).
[9] Y.H. Jo, S. Jung, W.M. Choi, S.S. Sohn, H.S. Kim, B.J. Lee, N.J. Kim, S. Lee, Nat. Commun. 8 (2017) 1–8.
[10] R. Feng, C. Zhang, M.C. Gao, Z. Pei, F. Zhang, Y. Chen, D. Ma, K. An, J. D. Poplawsky, L. Ouyang, Y. Ren, J.A. Hawk, M. Widom, P.K. Liaw, Nat. Commun. 12 (2021) 6–15.
[11] D.B. Miracle, O.N. Senkov, Acta Mater. 122 (2017) 448–511.
[12] Y.F. Ye, Q. Wang, J. Lu, C.T. Liu, Y. Yang, Mater. Today 19 (2016).
[13] T. DebRoy, H.L. Wei, J.S. Zuback, T. Mukherjee, J.W. Elmer, J.O. Milewski, A. M. Beese, A. Wilson-Heid, A. De, W. Zhang, Prog. Mater. Sci. 92 (2018) 112–224.
[14] S. Bose, D. Ke, H. Sahasrabudhe, A. Bandyopadhyay, Prog. Mater. Sci. 93 (2018) 45–111.
[15] N.T. Aboulkhair, M. Simonelli, L. Parry, I. Ashcroft, C. Tuck, R. Hague, Prog. Mater. Sci. 106 (2019), 100578.
[16] A. Talignani, R. Seede, A. Whitt, S. Zheng, J. Ye, I. Karaman, M.M. Kirka, Y. Katoh, Y.M. Wang, Addit. Manuf. 58 (2022), 103009.
[17] L. Zhao, L. Song, J.G. Santos Macías, Y. Zhu, M. Huang, A. Simar, Z. Li, Addit. Manuf. 56 (2022), 102914.
[18] L. Yan, Y. Chen, F. Liou, Addit. Manuf. 31 (2020), 100901.
[19] H.R. Kotadia, G. Gibbons, A. Das, P.D. Howes, Addit. Manuf. 46 (2021), 102155.
[20] G.M. Volpato, U. Tetzlaff, M.C. Fredel, Addit. Manuf. 55 (2022).
[21] C. Han, Q. Fang, Y. Shi, S.B. Tor, C.K. Chua, K. Zhou, Adv. Mater. 32 (2020) 1–41.
[22] P. Kürnsteiner, M.B. Wilms, A. Weisheit, B. Gault, E.A. Jägle, D. Raabe, Nature 582 (2020) 515–519.
[23] D. Zhang, D. Qiu, M.A. Gibson, Y. Zheng, H.L. Fraser, D.H. StJohn, M.A. Easton, Nature 576 (2019) 91–95.
[24] J.H. Martin, B.D. Yahata, J.M. Hundley, J.A. Mayer, T.A. Schaedler, T.M. Pollock, Nature 549 (2017) 365–369.
[25] J. Suryawanshi, K.G. Prashanth, S. Scudino, J. Eckert, O. Prakash, U. Ramamurty, Acta Mater. 115 (2016) 285–294.
[26] N. Sanaei, A. Fatemi, Prog. Mater. Sci. 117 (2021), 100724.
[27] U. Zerbst, G. Bruno, J.Y. Buffière, T. Wegener, T. Niendorf, T. Wu, X. Zhang, N. Kashaev, G. Meneghetti, N. Hrabe, M. Madia, T. Werner, K. Hilgenberg, M. Koukolíková, R. Procházka, J. Džugan, B. Möller, S. Beretta, A. Evans, R. Wagener, K. Schnabel, Prog. Mater. Sci. 121 (2021) 1–73.
[28] C.S. Montross, T. Wei, L. Ye, G. Clark, Y.W. Mai, Int. J. Fatig. 24 (2002) 1021–1036.
[29] C. Ye, S. Suslov, B.J. Kim, E.A. Stach, G.J. Cheng, Acta Mater. 59 (2011) 1014–1025.
[30] H. Lu, Z. Wang, J. Cai, X. Xu, K. Luo, L. Wu, J. Lu, Corrosion Sci. 188 (2021), 109558.
[31] D. Lin, M. Motlag, M. Saei, S. Jin, R.M. Rahimi, D. Bahr, G.J. Cheng, Acta Mater. 150 (2018) 360–372.
[32] J.Z. Lu, L.J. Wu, G.F. Sun, K.Y. Luo, Y.K. Zhang, J. Cai, C.Y. Cui, X.M. Luo, Acta Mater. 127 (2017) 252–266.
[33] W. Fu, Y. Huang, J. Sun, A.H.W. Ngan, Int. J. Plast. 154 (2022), 103296.
[34] C. Zhang, Y. Dong, C. Ye, Adv. Eng. Mater. 23 (2021) 1–24.
[35] Z. Tong, H. Liu, J. Jiao, W. Zhou, Y. Yang, X. Ren, Addit. Manuf. 35 (2020), 101417.
[36] Z. Tong, H. Liu, J. Jiao, W. Zhou, Y. Yang, X. Ren, J. Mater. Process. Technol. 285 (2020), 116806.
[37] S. Plimpton, J. Comput. Phys. 117 (1995) 1–19.
[38] P. Hirel, Comput. Phys. Commun. 197 (2015) 212–219.
[39] Y. Mishin, M.J. Mehl, D.A. Papaconstantopoulos, Phys. Rev. B Condens. Matter 65 (2002) 1–14.
[40] S.M. Eich, D. Beinke, G. Schmitz, Comput. Mater. Sci. 104 (2015) 185–192.
[41] D. Farkas, A. Caro, J. Mater. Res. 35 (2020) 3031–3040.
[42] A. Stukowski, Model. Simulat. Mater. Sci. Eng. 18 (2010), 015012.
[43] P.M. Larsen, Sø Schmidt, J. SchiØtz, Model. Simulat. Mater. Sci. Eng. 24 (2016), 055007.
[44] S. Lou, Y. Li, L. Zhou, X. Nie, G. He, W. He, Mater. Des. 104 (2016) 320–326.
[45] Y. Yang, H. Zhang, H. Qiao, J. Alloys Compd. 722 (2017) 509–516.
[46] B. Jiang, A. Tu, H. Wang, H. Duan, S. He, H. Ye, K. Du, Acta Mater. 155 (2018) 56–68.
[47] C.Q. Chen, G. Hu, J.N. Florando, M. Kumar, K.J. Hemker, K.T. Ramesh, Scripta Mater. 69 (2013) 709–712.
[48] R.W. Armstrong, S.M. Walley, Int. Mater. Rev. 53 (2008) 105–128.
[49] L.M. Hsiung, D.H. Lassila, Acta Mater. 48 (2000) 4851–4865.
[50] Q.J. Li, H. Sheng, E. Ma, Nat. Commun. 10 (2019) 1–11.
[51] J.Z. Lu, K.Y. Luo, Y.K. Zhang, G.F. Sun, Y.Y. Gu, J.Z. Zhou, X.D. Ren, X.C. Zhang, L. F. Zhang, K.M. Chen, C.Y. Cui, Y.F. Jiang, A.X. Feng, L. Zhang, Acta Mater. 58 (2010) 5354–5362.
[52] J.Z. Lu, K.Y. Luo, Y.K. Zhang, C.Y. Cui, G.F. Sun, J.Z. Zhou, L. Zhang, J. You, K. M. Chen, J.W. Zhong, Acta Mater. 58 (2010) 3984–3994.
[53] Z. Tong, H. Liu, J. Jiao, W. Zhou, Y. Yang, X. Ren, J. Mater. Process. Technol. 285 (2020), 116806.
[54] S.N. Luo, T.C. Germann, T.G. Desai, D.L. Tonks, Q. An, J. Appl. Phys. 107 (2010), 123507.
[55] J. Hu, Z. Chen, Comput. Mater. Sci. 197 (2021), 110635.
[56] X. Pan, X. Wang, Z. Tian, W. He, X. Shi, P. Chen, L. Zhou, J. Alloys Compd. 850 (2021), 156672.
[57] X. Chen, Q. Wang, Z. Cheng, M. Zhu, H. Zhou, P. Jiang, L. Zhou, Q. Xue, F. Yuan, J. Zhu, X. Wu, E. Ma, Nature 592 (2021) 712–716.
[58] L.S. Tóth, Y. Estrin, R. Lapovok, C. Gu, Acta Mater. 58 (2010) 1782–1794.
[59] X. Wang, T. Li, Y. Gao, Extrem. Mech. Lett. 48 (2021), 101413.